Newcastle University

ePrints

Andrews SB, Moore P, King MA.

Mass change from GRACE: a simulated comparison of Level-1B analysis techniques.

***Geophysical Journal International* 2015,200(1), 503-518.**

Copyright:

© The Authors 2014. Published by Oxford University Press on behalf of The Royal Astronomical Society.

This is an Open Access article distributed under the terms of the Creative Commons Attribution License (http://creativecommons.org/licenses/by/4.0/), which permits unrestricted reuse, distribution, and reproduction in any medium, provided the original work is properly cited.

Link to published article:

http://dx.doi.org/10.1093/gji/ggu402

Date deposited:

19/02/2015

This work is licensed under a Creative Commons Attribution 4.0 International License

Newcastle University ePrints - eprint.ncl.ac.uk

Geophysical Journal International

Geophys. J. Int. (2015) **200,** 503–518
GJI Gravity, geodesy and tides

doi: 10.1093/gji/ggu402

Mass change from GRACE: a simulated comparison of Level-1B analysis techniques

Stuart B. Andrews,[1] Philip Moore[1] and Matt. A. King[1,2]

[1]*School of Civil Engineering and Geosciences, Newcastle University, Newcastle upon Tyne,* NE1 7RU*, United Kingdom.*
E-mail: s.b.andrews@newcastle.ac.uk
[2]*School of Land and Food, University of Tasmania, Private Bag* 76*, Hobart* 7001*, Australia*

Accepted 2014 October 13. Received 2014 October 10; in original form 2014 March 31

SUMMARY

Spherical harmonic and mascon parameters have both been successfully applied in the recovery of time-varying gravity fields from Gravity Recovery and Climate Experiment (GRACE). However, direct comparison of any mass flux is difficult with solutions generated by different groups using different codes and algorithms. It is therefore opportune to compare these methodologies, within a common software base, to understand potential limitations associated with each technique. Here we use simulations to recover a known monthly surface mass distribution from GRACE KBRR data. The ability of spherical harmonic and mascon parameters to resolve basin-level mass change is quantified with an assessment of how the noise and errors, inherent in GRACE solutions, are handled. Recovery of a noise and error free GLDAS anomaly revealed no quantifiable difference between spherical harmonic and mascon parameters. Expansion of the GLDAS anomaly to degree and order 120 shows that both spherical harmonic and mascon parameters are affected by comparable omission errors. However, the inclusion of realistic KBRR noise and errors in the simulations reveals the advantage of the mascon parameters over spherical harmonics at reducing noise and errors in the higher degree and order harmonics with an rms (cm of EWH) to the GLDAS anomaly of 10.0 for the spherical harmonic solution and 8.8 (8.6) for the 4°(2°) mascon solutions. The introduction of a constraint matrix in the mascon solution based on parameters that share geophysical similarities is shown to further reduce the signal lost at all degrees. The recovery of a simulated Antarctic mass loss signal shows that the mascon methodology is superior to spherical harmonics for this region with an rms (cm of EWH) of 8.7 for the 2° mascon solution compared to 10.0 for the spherical harmonic solution. Investigating the noise and errors for a month when the satellites were in resonance revealed both the spherical harmonic and mascon methodologies are able to recover the GLDAS and Antarctic mass loss signal with either a comparable (spherical harmonic) or improved (mascon) rms compared to non-resonance periods.

Key words: Inverse theory; Satellite geodesy; Gravity anomalies and Earth structure; Time variable gravity; Global change from geodesy; Antarctica.

1 INTRODUCTION

The Gravity Recovery and Climate Experiment (GRACE) twin satellite mission (Tapley *et al.* 2004b) was launched in 2002 with the aim of mapping the Earth's time-varying gravity (TVG) field every ∼30 days (Wahr *et al.* 2004) at spatial scales of hundreds of kilometres. GRACE consists of two near-polar satellites separated along-track by ∼220 km. This separation results in the two satellites experiencing small orbital perturbations, caused by local mass anomalies, at different times. It is through measuring the changing distance between the satellites, caused by these perturbations, that GRACE allows us to monitor spatial and temporal geophysical mass variations in the gravity field. The range between the satellites is measured using a K/Ka band instrument which has an accuracy of a few microns (Dunn *et al.* 2003). The first time-derivative provides a K/Ka band range rate (KBRR) measurement, which is generally used during GRACE data processing and has a precision of 0.1 μm s^{-1} (Luthcke *et al.* 2006b). The GRACE satellites are equipped with Global Positioning System (GPS) receivers to position the satellites and on-board accelerometers to measure the non-conservative forces that affect the satellites allowing, shortly after launch, the detection of changes in mass corresponding to 1.4 cm of equivalent water height (EWH) over a radius of 750 km every 30 days (Wahr *et al.* 2004). Analysis improvements have since driven this uncertainty/radius downward. The data from these instruments are available to the scientific community as Level-1B data, namely

© The Authors 2014. Published by Oxford University Press on behalf of The Royal Astronomical Society. This is an Open Access article distributed under the terms of the Creative Commons Attribution License (http://creativecommons.org/licenses/by/4.0/), which permits unrestricted reuse, distribution, and reproduction in any medium, provided the original work is properly cited.

Downloaded from http://gji.oxfordjournals.org/ at University of Newcastle on February 19, 2015

the raw satellite products after a low-pass filter and time correction (Chen *et al.* 2008).

The ability to accurately recover the Earth's temporal mass anomalies every 30 days to a few hundred kilometres allows the monitoring of global geophysical processes between successive 30 day solutions and provides a means to assess and improve geophysical models. GRACE data has been successfully used for estimating ice mass balance trends (e.g. King *et al.* 2012; Shepherd *et al.* 2012; Luthcke *et al.* 2013), hydrological change (e.g. Han *et al.* 2009; Awange *et al.* 2011; Ramillien *et al.* 2011), ocean mass variability (e.g. Chambers *et al.* 2010; Chambers & Bonin 2012), Glacial Isostatic Adjustment (GIA; e.g. Riva *et al.* 2009) and studying Earthquake displacements (Han *et al.* 2008). Without the spatial and temporal resolution provided by GRACE, the separation of the signals from many of these geophysical phenomena would not have been possible (Swenson & Wahr 2002).

Since the launch of GRACE several processing methodologies have been applied to the GRACE Level-1B data with the aim of estimating the temporal variations of mass anomalies while reducing the impact that noise and errors have on the solutions. The presence of north–south 'stripes' in the solution results from the limited longitudinal sampling of GRACE, which reduced observability of the sectorial and near-sectorial coefficients (Klees *et al.* 2008), and result from the orbital configuration of GRACE; the KBRR data are only collected along the line of the orbit. Stripes also suggest a high degree of correlation in the GRACE errors (Swenson & Wahr 2006). If not correctly dealt with, measurement and processing errors and unmodelled mass variations in the GRACE solution could be interpreted as real mass change (Wahr *et al.* 2006). Random and systematic errors, present in the instrument data and background models, can dominate the solution at short wavelengths and increase rapidly with the spherical harmonic degree (Klees *et al.* 2008) while errors in geophysical models can cause poor estimates of certain spherical harmonic coefficients and alias into the solutions (Seo *et al.* 2008). In addition, the ground coverage of the satellites also affects the quality of the solutions. Periods where the GRACE satellites are in near 3, 4 and 7 day repeat orbits modify the noise characteristics of the GRACE solutions (Save *et al.* 2012). Noise and errors in the GRACE solutions need to be appropriately treated and mitigated before any meaningful mass anomalies can be estimated.

The most common methodology used to estimate the temporal variations of mass anomalies is the recovery of spherical harmonic (Stokes') coefficients (Tapley *et al.* 2004b; Wahr *et al.* 2004). The GRACE data processing centres, namely Centre for Space Research (CSR), Jet Propulsion Laboratory (JPL) and GeoForschungs Zentrum (GFZ), each provide monthly estimates of the global TVG field in the form of spherical harmonic fields to degree and order 60–90. These Level-2 products are normally computed directly from Level-1B KBRR and GPS data, but Level-2 solutions have been successfully computed using GRACE KBRR data only (Luthcke *et al.* 2006a). Due to the complex nature and computational requirement of Level-1B data processing, Level-2 products are widely used by researchers who undertake studies of mass flux analysis. A number of post-processing strategies have been proposed to remove the noise and errors in the solutions including the use of Gaussian smoothing (e.g. Wahr *et al.* 1998, 2004; Tapley *et al.* 2004a), filtering using empirical orthogonal functions (EOF; e.g. Wouters & Schrama 2007), destriping (e.g. Swenson & Wahr 2006) and forward modelling (e.g. Wouters *et al.* 2008; Schrama & Wouters 2011). Gaussian smoothing is probably the most common processing strategy (Rowlands *et al.* 2010). Access to solution normal matrices allows users to constrain the higher degrees of the TVG fields to the mean field (e.g. Bruinsma *et al.* 2010; Save *et al.* 2012) but these are not typically provided as part of the Level-2 solutions and are only available to users generating solutions from Level-1B data.

Mass concentration (mascon) parameters, estimated using only GRACE Level-1B KBRR data, have also been applied to the modelling of TVG, primarily at the NASA Goddard Space Flight Centre (GSFC; Rowlands *et al.* 2005, 2010; Luthcke *et al.* 2006b, 2008; Sabaka *et al.* 2010). The estimation of mascon parameters, first applied by Muller & Sjogren (1968) to model lunar gravity variations, has allowed the Earth's TVG to be modelled at a spatial and temporal resolution unachievable using conventional spherical harmonics due to the embedded smoothing resulting in less signal loss (Rowlands *et al.* 2010). The mascon methodology benefits from constraint equations applied during the least squares inversion which removes the requirement of post-processing, making possible solutions with a 10 day temporal resolution and a spatial sampling of 4° or 2° (Rowlands *et al.* 2010) with the most recent published mascon solutions using a 1° spatial sampling (Luthcke *et al.* 2013). The mascon constraint matrix is anisotropic in nature as it can be applied to constrain distinct geographical regions while also taking into account the full noise covariance matrix (Luthcke *et al.* 2013). The use of mascon parameters has allowed basin scale interannual variability to be extracted from the GRACE time-series (Rowlands *et al.* 2010) due to the increased spatial sampling and temporal resolution of the solutions. Mascon TVG estimates, unlike spherical harmonic coefficients, can be either local or global in extent as the KBRR data associated with the mascon is dominated by mass flux below the satellite (Luthcke *et al.* 2008). Mascon parameters can be estimated from short arcs of KBRR data through the estimation of short arc baseline parameters (Rowlands *et al.* 2002). However this requires GRACE accelerometer data to deal with non-conservative forces and the satellite orbits to have been previously well determined using GNV1B (GPS Navigation Data Level-1B) positioning data. Estimating mascon parameters from Level-1B data is different from the mascons used in Jacob *et al.* (2012) and Schrama *et al.* (2014), where mascon parameters are calculated from Level-2 spherical harmonics data.

Both spherical harmonic and mascon methodologies are applied to the recovery of TVG, but most users of GRACE data are heavily reliant on pre-processed Level-2 spherical harmonic products. It is therefore important that an assessment of these methodologies is undertaken to provide users with an understanding of their associated limitations and to assess the ability of each technique to resolve basin-level mass changes at a variety of spatial scales. The need for this assessment is further compounded as these processing methodologies are applied by different groups using different codes and algorithms, making it hard to directly compare any subsequent mass flux analysis. Pritchard *et al.* (2011) highlighted that differences within Level-1B processing applied at different groups is the main source of the discrepancies in TVG solutions, with solutions generated using the same fundamental processing software agreeing within estimated errors (see also Shepherd *et al.* 2012).

While there are a limited number of studies which have compared different approaches within the same software base (e.g. Rowlands *et al.* 2010; Awange *et al.* 2011), no study, as far as we are aware, has been undertaken that simulates the recovery of a known signal using both mascon and spherical harmonic solutions within the same software. Accordingly, we undertake a comparison of solutions generated through the estimation of mascon parameters and spherical harmonic coefficients. Simulations will provide an

Downloaded from http://gji.oxfordjournals.org/ at University of Newcastle on February 19, 2015

accuracy assessment and quantify the capability of each technique to resolve basin-level mass changes at a variety of spatial scales while understanding how the methodologies handle the noise and errors inherent at higher degree and orders. Actual noise and errors, obtained during GRACE Level-1B data processing, will be used to create simulated stripes for use during the simulations. While we only simulate the recovery of a single signal, the assessment of the methodologies aims to provide users with an understanding of their associated limitations, as correctly recovering individual monthly solutions is imperative when using these solutions for deriving longer term trends.

We will use simulations to compare a mascon and spherical harmonic solution using a standard Gaussian smoothing filter for the post-processing of the spherical harmonic solution and a spatial constraint matrix applied to the mascon solution. The aim of this paper is to investigate the effect of the fundamental processing methodology applied to the GRACE Level-1B data on the recovered monthly time variable gravity field. It is worth noting that different post-processing strategies applied to the spherical harmonic solutions will generate different mass flux estimates, however only the difference in the fundamental Level-1B processing strategy will be considered in this work.

The outline of the paper is as follows. In Section 2 we describe the formation of mascon parameters before discussing the processing methodology in Section 3. The results of the simulations will be presented in Section 4. Throughout this paper special attention will be paid to the formation and behaviour of the mascon parameters to aid understanding of the methodology. Spherical harmonic solutions are widely dealt with in the literature and their estimation is not explicitly described here.

2 FORMATION OF THE MASCON PARAMETERS

The mascon parameters are based on the GSFC methodology which involves calculating a scaling factor for a set of 'delta' spherical harmonic coefficients that represent a uniform layer of surface mass over an area which can be added to the mean background field and used to represent the mass flux at a certain time. Rowlands *et al.* (2010) showed that the only difference between these differential coefficients is the shape, size and location of the area. Each separate area is a mascon as defined by estimating a scale factor $H(t)$ at time t for a uniform mass of one unit of EWH over the mascon area, namely

$$\delta^m(\phi,\lambda) = R_e\rho_w \left\{ \begin{array}{l} 1, \text{ over mascon} \\ 0, \text{ elsewhere} \end{array} \right\}, \quad (1)$$

where the mascon is centred on geodetic latitude ϕ, longitude λ; R_e is the radius of the Earth and ρ_w the density of fresh water (1000 kg m^{-3}).

In this paper, we use global equal area masons, where each mascon is rectangular in latitude and longitude spanning 2° or 4° in latitude with the longitude span selected to give approximately the same area as a 2° by 2° or 4° by 4° mascon located at the equator. While not strictly 2° by 2° or 4° by 4°, for simplicity we refer to them as such hereafter. The only exception is at the poles where polar caps of 2° in latitude are used. Due to the convergence of longitude at the poles, the number of mascons in a given latitude band will reduce poleward as seen in Fig. 1 for a grid of 2° mascons over Antarctica.

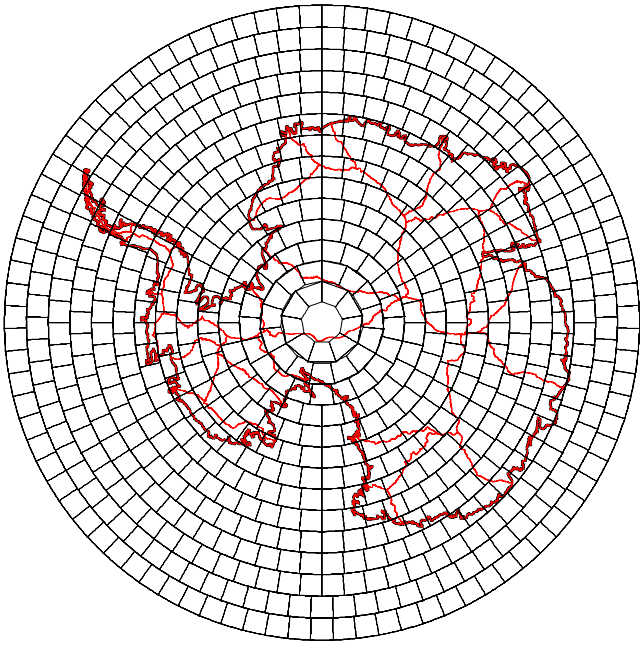

Figure 1. Distribution of 2° equal area mascons around Antarctica. Antarctic drainage basins (Zwally *et al.* 2012) are also shown (red).

Using eq. (1) each mascon in the grid can be expanded into spherical harmonics as

$$\delta^m(\phi,\lambda) = R_e\rho_w \sum_{l=0}^{l_{max}} \sum_{m=0}^{l} \left(\Delta\tilde{C}_{lm}^{(m)} \cos m\lambda + \Delta\tilde{S}_{lm}^{(m)} \sin m\lambda \right) \times \bar{P}_{lm}(\cos\phi), \quad (2)$$

where $\Delta\tilde{C}_{lm}^{(m)}$ and $\Delta\tilde{S}_{lm}^{(m)}$ are the dimensionless normalized surface harmonics and $\bar{P}_{lm}$ normalized associated Legendre polynomials. The sum over degree l and order m in eq. (2) is truncated to $l_{max} = 60$. We utilize eq. (2) to modify eqs (11) and (12) of Wahr *et al.* (1998) to obtain (delta) spherical harmonic gravitational coefficients, $\Delta C_{lm}^{(m)}$ and $\Delta S_{lm}^{(m)}$, that describe the required mass spread uniformly over a global set of mascons to give

$$\Delta C_{lm}^{(m)} = H(t)\frac{3\rho_w}{4\pi R_e\rho_{av}}\frac{1+k_l}{2l+1}\Delta\tilde{C}_{lm}^{(m)}$$

$$\Delta S_{lm}^{(m)} = H(t)\frac{3\rho_w}{4\pi R_e\rho_{av}}\frac{1+k_l}{2l+1}\Delta\tilde{S}_{lm}^{(m)}. \quad (3))$$

In eq. (3), ρ_{av} is the average density of the Earth ($\frac{5517\,\text{kg}}{\text{m}^3}$) and k_l the load Love number of degree l (Farrell 1972) to account for the deformation of the load on an elastic Earth. The mascon parameter (H) is a scale factor of the spherical harmonic coefficients used to describe that mascon (Rowlands *et al.* 2010). During the orbital integration we use the spherical harmonic coefficients from eq. (3) to calculate H by least-squares utilizing the partial derivatives of the KBRR observation data (*cf.* Luthcke *et al.* 2013), that is

$$A_{IJ} = \frac{\partial KBRR_I}{\partial H_J} = \sum_{l=1}^{l_{max}} \sum_{m=0}^{l} \frac{\partial KBRR_I}{\partial \Delta C_{lm}^J}\frac{\partial \Delta C_{lm}^J}{\partial H_J} + \frac{\partial KBRR_I}{\partial \Delta S_{lm}^J}\frac{\partial \Delta S_{lm}^J}{\partial H_J}, \quad (4)$$

where A_{IJ} are elements of the design matrix, $\partial KBRR_I/\partial H_J$ is the partial derivative of the KBRR observation i with respect to the mascon parameter j, $\partial KBRR_I/\partial \Delta C_{lm}^J$ and $\partial KBRR_I/\partial \Delta S_{lm}^J$ are

Downloaded from http://gji.oxfordjournals.org/ at University of Newcastle on February 19, 2015

the partial derivatives of the KBRR observations with respect to the delta gravitational coefficients while $\partial \Delta C^J_{lm}/\partial H_J$ and $\partial \Delta S^J_{lm}/\partial H_J$ are the partial derivatives of the delta gravitational coefficients with respect to the mascon parameter j. Let $\underline{\hat{x}}$ be the least squares solution to the KBRR linearized observation equations $A\underline{x} - \underline{b} - \underline{v}_1 = \underline{0}$ with observation weight matrix W and Gaussian error $\underline{v}_1$. The solution vector $\underline{\hat{x}}$ includes GRACE orbital parameters and either mascon parameters, H, or corrections ΔH to mascons parameters H_k at the k^{th} stage of an iterative procedure (*cf.* Sabaka *et al.* 2010). The vector $\underline{b}$ is formed from the KBRR calculated minus observed residuals. Analogously, we incorporate spatial and temporal constraints on the mascons through pseudo-observations $C\underline{x} - \underline{q} - \underline{v}_2 = \underline{0}$ with weight matrix V, where $\underline{q}$ is a constant vector incorporating both non-zero constraints and the component $-CH_k$ if the procedure is iterative. Then, $\underline{\hat{x}}$ is obtained from

$$(A^T W A + C^T V C)\underline{\hat{x}} = A^T W \underline{b} + C^T V \underline{q}. \tag{5}$$

The matrix, C, incorporates the mascon spatial and/or temporal constraints. For mascons, J_1, J_2, with the same geophysical property the pseudo-observations can be written as

$$H_{J_1} - H_{J_2} = 0, \tag{6}$$

where $J_1 \neq J_2; J_1, J_2 \in A_k$, the kth mascon region. Additional pseudo-observations are applied to ensure total mass is conserved (equivalent to a degree 0 term) and that the degree 1 harmonics for surface mass are zero; GRACE is insensitive to degree 1 harmonics as the satellites orbit around the instantaneous centre of mass. The inclusion of background models during the orbital integration could result in non-zero degree 1 terms and mass not being conserved in the solution vector without the use of pseudo-observations; individual models do not conserve mass and may give non-zero degree 1 coefficients (Wahr *et al.* 1998). The degree 0 and 1 pseudo-observations are prescribed a high weight in V to ensure the solution essentially satisfies these conditions. The four constraint equations for degrees $l = 0$, 1 and order $m = 0$, 1 are of the form

$$\sum_J H_J \Delta C^{(J)}_{l,m} = -\Delta C^{(\text{atmos})}_{l,m} - \Delta C^{(\text{ocean})}_{l,m}, \tag{7}$$

where the summation is over all mascons and $\Delta C^{(\text{atmos})}_{l,m}$ and $\Delta C^{(\text{ocean})}_{l,m}$ are the harmonics from the GRACE dealiasing product for the ocean and atmosphere. By stipulating eq. (7), the total contribution due to the mascons for the degree 0 and 1 harmonics will offset the *a priori* mass of the ocean and atmosphere if used in the GRACE computations, giving zero values for these harmonics at all times.

The weight matrix V utilizes constraints between the mascon parameters,

$$V_{IJ} = S \times \mathrm{e}^{\left(2 - \frac{d_{IJ}}{D} - \frac{t_{IJ}}{T}\right)}, \tag{8}$$

where d_{IJ} is the distance in kilometres between the mascons, D the correlation distance, t_{IJ} the time difference in days between the solutions, T the correlation time and S a scale factor. The scale factor is required to ensure that the constraints are in proportion to the normal matrices. Setting the constraint too small will not substantially reduce the noise and error in the solution, while adding a large constraint will oversmooth the signal and remove both noise and error and real signal (Klosko *et al.* 2009). The value used for S, to be discussed later, depends on the units used for the normal matrices and constraint matrix. In Section 4.5, we found $S = 0.001$, the value used by Lemoine *et al.* (2007) and Rowlands *et al.* (2010), to be the optimal scale factor for the simulations. Values of $S = 0.01$ and $S = 0.0001$ were tested but were found to over/under constrain the simulated solutions. However, the choice of S is dependent on the values chosen for other parameters in eqs (8) and (9) as the weight matrix V is affected by the values assigned to S, D and T in eqs (8) and (9). The same scale factor is used for all constraints in the V matrix.

The need for temporal smoothing increases as the number of days included in the mascon solution increases. For consistency with the spherical harmonic approach, no temporal constraint is applied to the mascon monthly solutions presented here, leading to a modified version of the constraint matrix, namely

$$V_{IJ} = S \times \mathrm{e}^{\left(1 - \frac{d_{IJ}}{D}\right)}. \tag{9}$$

In our solutions, constraints are applied between all mascon pairs of the same type (land or ocean), but no constraint is applied between a pair consisting of a land and an ocean mascon. The constraint matrix can be easily modified to allow different constraints between pairs of mascon, as we will show in Sections 4.6 and 4.7.

3 SIMULATED DATA PROCESSING STRATEGY

During simulations we aim to recover a known surface mass distribution from GRACE KBRR data using Newcastle University's orbit determination software *Faust* (Moore *et al.* 1999). We compute the effect of the surface mass distribution through a spherical harmonic expansion to a specified degree and order, with the resultant gravitational field added to the mean GIF48 field (Ries *et al.* 2011), from which simulated noise and error free KBRR tracking data are computed. The simulations then attempt to recover the known signal from the tracking data up to degree and order 60. The normal equations from each arc, here taken as 60 min, were combined to create monthly solutions for the two methodologies. We only use KBRR data in our solutions as Luthcke *et al.* (2006a) showed that the gravity field can be successfully recovered from KBRR data using spherical harmonic parameters while estimating the Rowlands *et al.* (2002) short arc baseline parameters. Mascon parameters are usually estimated using only KBRR data. The use of KBRR data only removes the computational requirement of processing the GPS data which can weaken and corrupt the KBRR measurement if not handled correctly (Luthcke *et al.* 2006a).

Within our simulations, the only difference between the two processing strategies is the gravity field parameters being estimated (spherical harmonic or mascon). Thus, the underlying processing is the same for the two methodologies to the extent that any differences in the solution will be directly due to the parametrization (Rowlands *et al.* 2010) and how noise and errors propagate into the solutions. Mathematically the two methodologies are equivalent (Sabaka *et al.* 2010).

The choice of arc length was based on experimentation in deriving gravity field solutions using KBRR (and accelerometer) data with the satellite state vectors estimated simultaneously using the short baseline parameters. No GPS/GNV1B data or empirical parameters are required to stabilize the solutions. Analysis of 4 months of solutions revealed that the average fit of the KBRR residuals was 0.32 μm s^{-1} using 60 min arcs and 0.31 and 0.41 μm s^{-1} for 30 min and 90 min arcs, respectively. The 60 min arcs were favoured over the 30 min arcs due to the reduction in storage requirement. 24 hr arcs were used to calculate the GRACE accelerometer bias values before recovery of the gravity field parameters. Alongside the accelerometer biases, these runs estimate the full state vector

Downloaded from http://gji.oxfordjournals.org/ at University of Newcastle on February 19, 2015

from KBRR, GNV1B and accelerometer data while using empirical parameters to absorb unmodelled KBRR measurement variations for quality control purposes.

The results presented in Section 4.2 for a noise and error free simulation show that we are able to create KBRR tracking data that describes a simulated mass. Noise and errors are included in the simulation in Section 4.5, through creation of simulated stripes, allowing us to examine how the solutions differ at higher degree and orders using the different methodologies.

4 SIMULATIONS

4.1 Effect of a simulated mass on observed KBRR residuals

To understand the performance of the two methodologies a number of experiments were undertaken. The first experiment examined the effect of a simulated mass on the KBRR data. The simulated mass was created by loading a 4° block at the equator, described from spherical harmonic degree and order 2–60, with 30 cm of EWH. The spherical harmonic expansion was added to the mean background field to create error free KBRR tracking data. The effect of the mass on the KBRR residuals is plotted in Fig. 2, with $t = 0$ at the centre of the block. The simulation was repeated with the source mass loaded with 10 cm of EWH. The boundary of the 4° block is plotted giving a spatial domain ∼440 km in diameter.

Fig. 2 shows that both simulated masses modify the KBRR residuals inside and outside the source area as found by Rowlands *et al.* (2010). The largest KBRR values are observed at the boundary of the source area with a change from positive to negative as the GRACE satellite pair move over the centre. Either side of the source area is an extensive tail revealing that GRACE is sensitive to mass over a large area. Spatially, Fig. 2 covers an area of ∼2500 km. The amplitude and extent of the tail is a function of the size of the mass anomaly. Seo *et al.* (2006) found that the distribution of leakage is concentrated in regions with high hydrological variability. As the hydrology component is the largest seasonal signal in the GRACE data, Fig. 2 shows mass signal leakage from the source area into surrounding areas. These results, and the findings of Seo *et al.* (2006), lead to the conclusion that forward modelling of the hydrology signal will reduce the leakage in the GRACE signal as seen in Sabaka *et al.* (2010). However, as this assumes that sufficiently accurate models are available, forward modelling of hydrology will not be considered in this paper. The simulation was repeated with the source area described to spherical harmonic degree and order 120 (not shown). The results reveal that the additional degree and order 61–120 has minimal effect on KBRR residuals confirming the result seen in Rowlands *et al.* (2010).

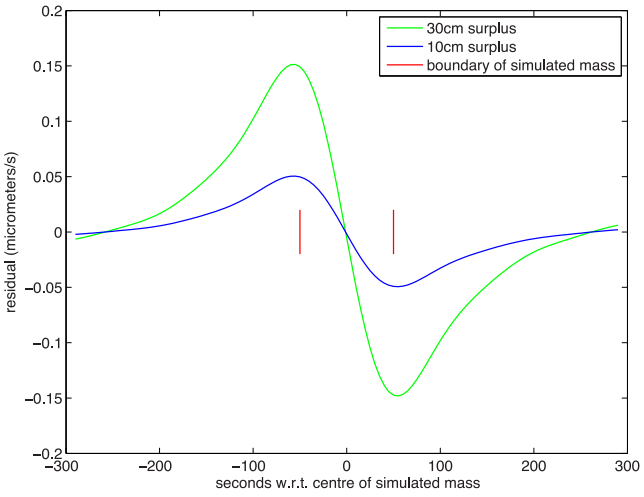

Figure 2. The residuals resulting from the 4° block loaded with 30 cm of EWH (green) and 10 cm of EWH (blue). The boundary of the simulated mass (red) is plotted for reference.

4.2 Simulated recovery of the GLDAS anomaly

The next simulation was the recovery of a known gravity signal through estimation of spherical harmonic and 2° and 4° mascon parameters to assess the performance of the different methodologies in an ideal case. The introduced signal was the June 2006 Global Land Data Assimilation System (GLDAS) Version 1 (Rodell *et al.* 2004) anomaly to the 2003–2010 mean derived from monthly averaged data with a 1° spatial resolution. Since hydrology is the largest seasonal contribution to the GRACE signal we are simulating the recovery of the main spatial and temporal variation, with similar characteristics to that contained within real GRACE data. We scaled the GLDAS anomaly upwards so the degree variances contained a similar power as the June 2006 CSR release 5 Level-2 field (Bettadpur 2012), as not all geophysical signal is present in the GLDAS anomaly. The GLDAS anomaly was derived to degree and order 60 and 120 (Fig. 3) with tracking data created from the different harmonic expansions. As the degree variances are identical up to degree and order 60, recovery of the GLDAS anomaly described to degree and order 120 allows us to observe how parameter estimation is affected by omission errors. Gravity field recovery was undertaken, for both GLDAS anomaly models, through

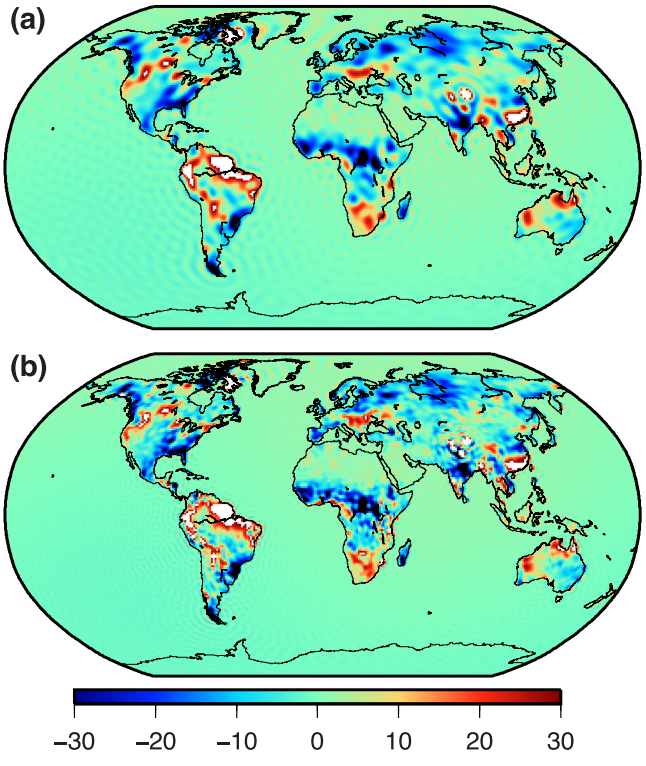

Figure 3. GLDAS mass anomaly for June 2006 as differenced from the 2003 to 2010 mean to degree and order 60 (a); degree and order 120 (b). Note that there is no GLDAS signal in Antarctica or Greenland or over the oceans. Units of cm of EWH.

Downloaded from http://gji.oxfordjournals.org/ at University of Newcastle on February 19, 2015

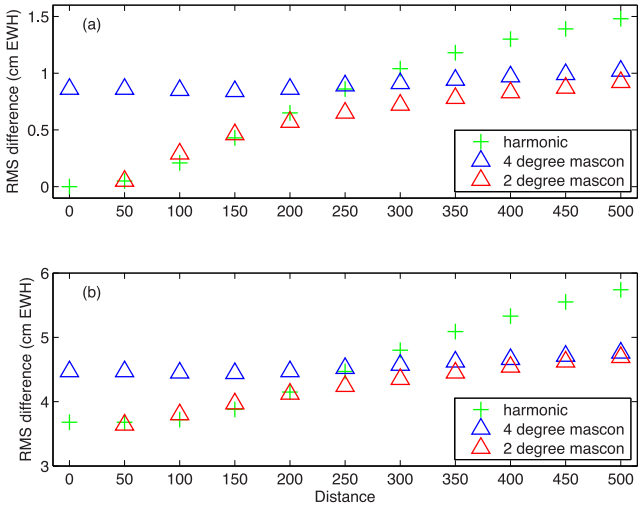

Figure 4. Rms of the differences between the calculated gravity field solutions and the noise and error free GLDAS anomaly in cm of EWH. GLDAS described to degree and order 60 (a); and degree and order 120 (b). The distance refers to the Gaussian smoothing radius (spherical harmonic coefficient solution) or the correlation distance (mascon solutions). The distance used in the mascons solutions (triangles) is not directly comparable to that used in the harmonic solution (crosses) and do not equate to the same smoothing radius.

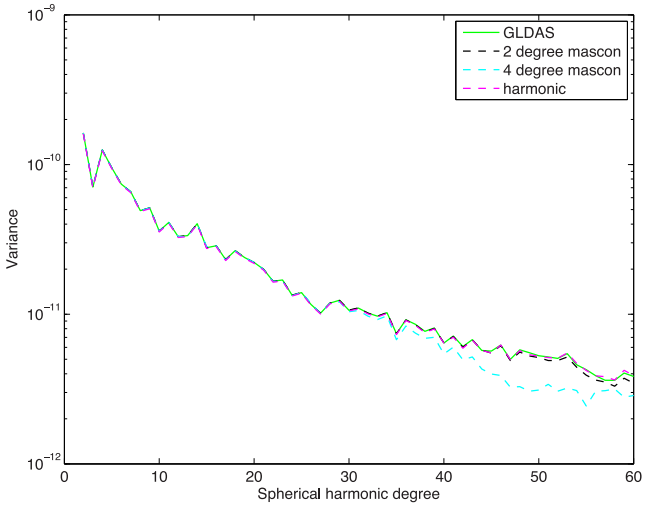

Figure 5. Degree variances of the spherical harmonic and mascon solutions. The degree variances of the noise and error free input GLDAS anomaly are included for comparative purposes.

spherical harmonic estimation to degree and order 60 (3717 parameters) while the 4° (2°) equal-area mascon solutions involved estimation of 2564 (10 292) mascon parameters. The monthly solution was collated from the individual 60 min arcs. No noise or errors were added to the solution at this stage.

Fig. 4(a) shows the rms in cm of EWH of the recovered anomaly to the input GLDAS data, described to degree and order 60. This is the ideal case. The rms is provided for various smoothing distances. For spherical harmonic coefficients the distance refers to the Gaussian smoothing radius, while for the mascon solutions the distance is D of eq. (9). As such, the two distances are not directly comparable as they do not equate to the same smoothing radius. The distance 0 km indicates that no Gaussian smoothing has been applied or that the mascon solutions are unconstrained.

Fig. 4(a) reveals that, without Gaussian smoothing, the spherical harmonic solution is able to exactly recover the reference degree and order 60 GLDAS anomaly using perfect data. Adding Gaussian smoothing dampens the amplitude of the recovered signal. For the 4° mascon solution, the smallest rms is obtained when a correlation distance of 150 km is used in the constraint matrix, but the solution is not able to fully recover the input GLDAS anomaly. This is to be expected as the GLDAS anomaly was expanded to spherical harmonics degree and order 60 (3717 gravity field parameters) while the 4° mascon solution involves estimation of 2564 mascon parameters. The recovery favours the spherical harmonic solution over the 4° mascon solution with the latter unable to recover the gravity field. The use of the constraint matrix in the mascon solution does enable a small improvement in the ability to recover this short wavelength signal.

The 2° mascon solution involves estimation of 10 292 mascon parameters and consequently nearly a factor 4 more parameters than the spherical harmonic solution. If no constraint matrix is applied, the solution does not invert as it is rank deficient by a large margin (Rowlands *et al.* 2010). Adding a constraint matrix with ≥50 km correlation distance stabilizes the solution and allows recovery of the GLDAS anomaly. The resulting rms to the input GLDAS anomaly is 0.05 cm of EWH, which is the same as the spherical harmonic recovery with 50 km Gaussian smoothing. Increasing the correlation distance in the constraint matrix increases the effect of the constraint matrix and over constrains the mascon solution, reducing high frequency signal.

Fig. 4(b) shows the rms of the recovered anomaly to the input GLDAS data, described to degree and order 120. This allows us to compare the effect of omission errors on the different parameters. The pattern is similar to the ideal case (GLDAS to degree and order 60), but with an increase in all rms values. Methodologies that are essentially truncated to degree and order 60 are, of course, unable to fully recover an input signal described to degree and order 120 and hence unable to capture the additional short wavelength (high degree) information.

Fig. 5 shows the degree variances of the spherical harmonic and mascon solutions to degree 60. The degree variance of the input GLDAS anomaly is included for reference. All three solutions match the degree variance of the input GLDAS anomaly to near degree 40 from where the 4° mascon solution loses power. This reduction is the result of the under sampling of the input signal by the 4° mascon solution. The spherical harmonic coefficient and 2° mascon solutions are able to replicate the degree variances of the GLDAS anomaly. The slight reduction in power at degree ∼55–60 in the 2° mascon solution is the result of the 50 km correlation distance used in the constraint matrix to stabilize the inversion. The ability of the spherical harmonic and 2° mascon solutions to replicate the degree variances of the GLDAS anomaly up to degree 60 in Fig. 5 shows that we are able to reproduce a known input signal from the simulated KBRR tracking data, validating the processing methodology. For the remainder of the paper, all processing uses the GLDAS anomaly described to degree and order 120 and hence allows consideration of omission errors.

4.3 Mascon centre-to-centre distance

As part of the evaluation of the force model the contribution of every mascon to the accelerations of the satellites is calculated. Thus, as for spherical harmonics, mascon solutions presented so far are global in extent with the drawback of added computational expense, at least in the case of the 2° mascon solutions. Fig. 2

Downloaded from http://gji.oxfordjournals.org/ at University of Newcastle on February 19, 2015

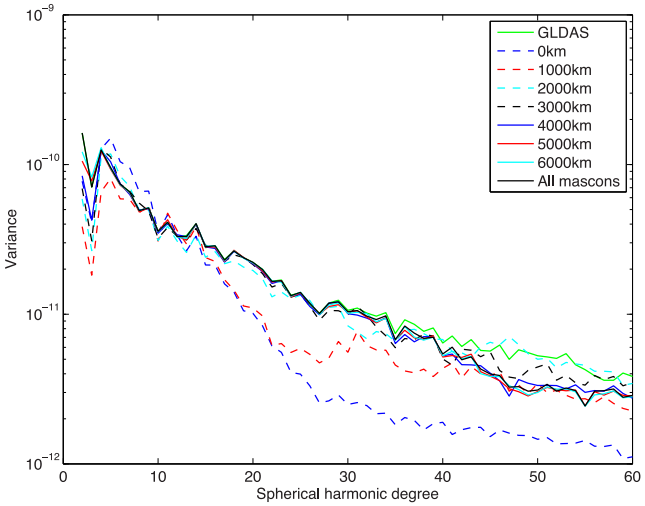

Figure 6. Degree variances of the 4° mascon solutions for a range of centre-to-centre cut-off distances. The degree variances of the input GLDAS anomaly (solid green) and original solution (solid black) are included for reference. All solutions here are noise and error free.

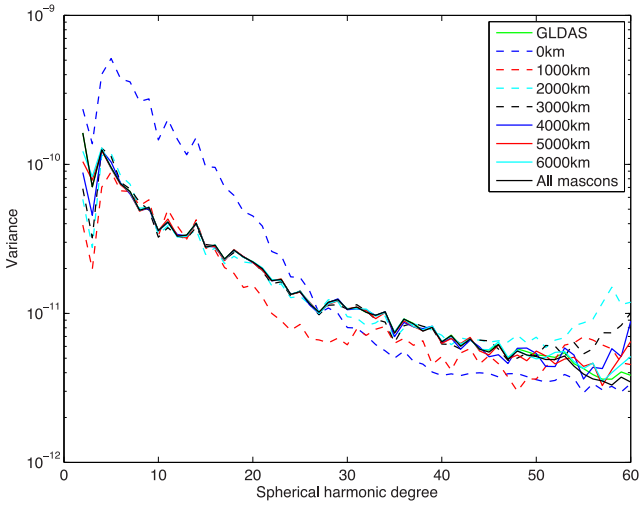

Figure 7. Degree variances of the 2° mascon solutions for a range of centre-to-centre cut-off distances. The degree variances of the input GLDAS anomaly (solid green) and original solution (solid black) are included for reference. All solutions here are noise and error free.

revealed that a mass anomaly leaks outside of the source area, and by extension neighbouring mass anomalies will leak into the source area. Fig. 2 also showed that this leakage is not global, but spatially limited. The limited spatial extent of a mass anomaly on gravitation experienced at the satellite altitude was noted by Velicogna & Wahr (2006). This suggests that we can achieve an adequate approximation of the total contribution of all mascons to the satellite accelerations by considering a reduced subset of mascons. This will allow estimation of a local mascon solution and reduce the computational requirement in a global solution.

To investigate this we repeated the simulated recovery of the GLDAS anomaly in Section 4.2, but this time we estimate only the contributions to the satellite accelerations of a subset of mascons. The number of mascons included is based on the distance between the centre of the mascon under consideration to the mascon directly below the leading GRACE satellite. We will call this the centre-to-centre distance and the mascon below the satellite the nadir mascon. Any mascon pair where the centre-to-centre distance is greater than a prescribed value will be excluded from eq. (4) and its effect set to zero. Thus, for each arc only a subset of mascons will be included in the normal equations, reducing the processing time and storage requirement. All the individual arcs will be summed to calculate a monthly solution, as previously. The solutions are global in extent as each month all mascon parameters are estimated in the monthly solution. Mascon 4° and 2° solutions were generated using various centre-to-centre distances. The resulting degree variances are plotted in Figs 6 and 7, respectively and compared to those from the global mascon solutions and input GLDAS anomaly. The 0 km centre-to-centre distance solution refers to the contribution of the nadir mascon only to the acceleration experienced by the GRACE satellites.

Fig. 6 reveals that for a centre-to-centre cut-off distance of 1000 km or less the degree variances of the original mascon solution are not well recovered as the leakage seen in Fig. 2 has not been fully accounted for. All such solutions have reduced power at higher degrees, which dampens short wavelength information in the gravity fields. The 0 km centre-to-centre distance solution in Fig. 7 (2° mascon) is anomalous with more power than expected, especially at lower degrees due to the leakage of the spherical harmonics used to define the mascon parameters in eq. (3). In both Figs 6 and 7,

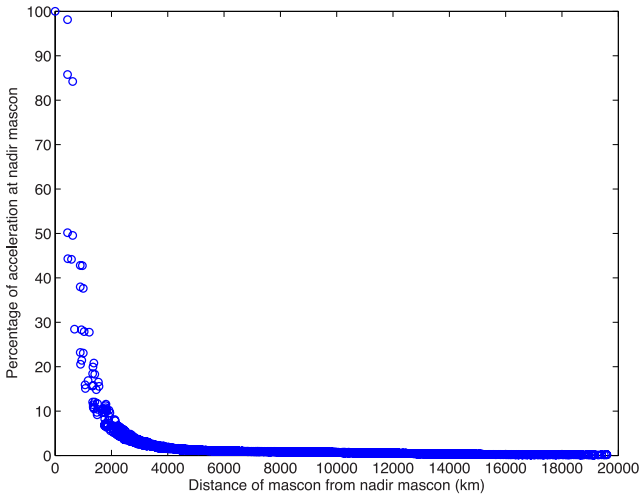

Figure 8. The contribution of mascons to the gravitational acceleration of a satellite over the Amazon as a function of the centre-to-centre distance. Acceleration is given as a percentage of the acceleration of the nadir mascon.

increasing the centre-to-centre distance to 6000 km improves the fit of the degree variances with the original mascon solution, at which point the degree variances for both the 2° and 4° mascon solutions closely resemble the global solution. A centre-to-centre distance of 4000 km or 5000 km could be used, but the solutions have less power at degree 2 and 3 harmonics (longer wavelength).

The contribution to the acceleration experienced by the GRACE satellites at distances from the nadir mascon are plotted in Fig. 8, for a nadir mascon located in the Amazon (similar results are observed when the nadir mascon is located elsewhere). The accelerations are given as a percentage of the acceleration of the nadir mascon. Fig. 8 reveals that, as expected, mascons close to the nadir mascon have a larger contribution to the accelerations experienced by the satellites than distant mascons. As the centre-to-centre distance increases, the contribution to the satellite acceleration reduces and approaches zero. Mascons within a centre-to-centre distance of up to 2000 km have the greatest contribution but mascons 2000 km from the nadir mascon still contribute ∼10 per cent of the acceleration of the nadir mascon. Mascons with centre-to-centre distances up to 4000 km are

Downloaded from http://gji.oxfordjournals.org/ at University of Newcastle on February 19, 2015

still seen to influence the accelerations experienced by the satellites. Above 4000 km the contributions to the accelerations reduce, explaining the relatively small improvements at higher degrees seen in Figs 6 and 7. A centre-to-centre cut-off distance of 6000 km will be used in future processing as the difference between that and a full global solution is minimal.

4.4 Iteration of the mascons

In Section 4.3 a good approximation to a true mass anomaly (simulated with GLDAS) was obtained by including the contribution of all mascons within a centre-to-centre distance of 6000 km. However, it is also worth investigating if a similar approximation can be achieved by using a smaller centre-to-centre cut-off distance but also iterating the solution. Iteration was shown by Luthcke *et al.* (2013) to substantially increase signal recovery. Here, we computed an iterated 4° mascon solution for the centre-to-centre distances of 0, 1000 and 2000 km and computed the rms of the differences to the known GLDAS anomaly (Table 1). The rms of the differences for the 3000, 4000, 5000 and 6000 km centre-to-centre solutions are also provided (not iterated) for comparison.

Table 1 shows that, while iterating will improve the solution, the extent of the improvement is limited. For iterated solutions convergence is normally reached by ∼5 steps. The rms improves with an increase in the centre-to-centre distance of the solution through to 6000 km at which the difference in the rms is only 0.06 cm of EWH to the original (all mascon) solution. A similar result is observed for more limited testing of the 2° solution (not shown). Iterations improve the solution but are not a substitute for using an appropriate centre-to-centre cut-off distance and our simulations show iterations were unable to overcome modelling deficiencies associated with an insufficient distribution of mascons when using perfect data. Iterations will therefore not be used in the remainder of this paper. Note that this iterative procedure is not intended as a study of the use of iterating a correctly parametrized solution. Applying iterations to real GRACE observations, as discussed in Luthcke *et al.* (2013), would be expected to yield improvements due to the separation of signal and noise through enhanced quality control of the residuals. Sabaka *et al.* (2010) found that forward modelling improved signal recovery while resulting in KBRR residuals that conformed more closely to zero-mean Gaussian distributions.

Table 1. Rms of the differences between the iterated 4° mascon solutions and the input GLDAS anomaly in cm of EWH. Rms values are provided over land (and globally). The inclusion of a mascon into the solution depends on the distance between that mascon and the nadir mascon being lower than the centre-to-centre distance.

Centre-to-centre distance (km)	Iteration number	Rms difference to GLDAS anomaly (cm EWH)
0	1	10.5 (6.4)
	2	10.3 (6.1)
	3	9.9 (6.0)
	4	9.8 (5.9)
	5	9.7 (6.0)
	6	9.8 (6.0)
	7	9.8 (6.2)
	8	9.9 (6.3)
1000	1	10.4 (6.2)
	2	10.1 (6.2)
	3	9.9 (6.2)
	4	9.8 (6.2)
	5	9.8 (6.3)
	6	9.8 (6.4)
	7	9.8 (6.5)
	8	9.9 (6.7)
2000	1	9.3 (5.9)
	2	9.1 (5.8)
	3	8.8 (5.6)
	4	8.7 (5.5)
	5	8.6 (5.5)
	6	8.6 (5.5)
	7	8.6 (5.5)
	8	8.6 (5.5)
3000	1	8.3 (5.2)
4000	1	7.7 (4.7)
5000	1	7.6 (4.6)
6000	1	7.5 (4.5)
All mascons	1	7.4 (4.4)

4.5 Simulated recovery of the GLDAS anomaly with simulated stripes

Computations to this point utilized noise and error free data. We now test the effect of adding realistic noise and errors to the simulated KBRR observations generated from observed noise and errors in processing actual GRACE data. Although not directly pertinent to the simulations we outline our current two stage processing strategy for GRACE data as the first stage provides the accelerometer bias values and state vectors for the short-arc gravity field recovery in the second stage. The accelerometer bias runs are undertaken in 24 hr arcs. In addition to constant accelerometer biases we also estimate the full state vector for GRACE A and B from KBRR, GNV1B and accelerometer data in addition to KBRR bias, trend and once and twice per rev per orbital revolution (16 sets per arc) measurement parameters. This process essentially computes the acceleration biases from the GNV1B Cartesian coordinates while the KBRR parameters account for unmodelled force effects enabling bad data to be identified.

To generate the KBRR noise and errors we re-processed the accelerometer runs estimating now 96 sets of empirical once per rev acceleration parameters along-track and cross-track instead of the KBRR parameters. The empirical accelerations absorbed the longer wavelength gravity field mismodelling with the KBRR residuals representing a realistic sample of the noise and errors present in the GRACE data. The empirical acceleration once per rev parameters also lead to slightly different values for the accelerometer biases values and estimated state vectors. The small differences in the accelerometer bias values between the runs are assumed to be similar to the differences between the original values and the unknown 'true' values. Similarly the orbit used to calculate the KBRR residuals will be different to the orbits used in the gravity recovery due to the use of different empirical parameters. The KBRR residuals time-series will also contain errors in the orbit introduced from the inclusion of the GNV1B data as well as the KBRR data (GNV1B data is not used in the 60 min arcs for gravity recovery). Furthermore, the KBRR residuals will also contain effects of aliasing of short period signals and errors in the background models which will affect the real GRACE solution. AOD1B (Atmosphere and Ocean de-aliasing Level-1B) product and the GLDAS anomaly field were utilized in all computations.

Despite best efforts it is likely that residual geographical correlated terms are present in the KBRR residuals due to the parametrization failing to absorb all gravity field mismodelling.

Downloaded from http://gji.oxfordjournals.org/ at University of Newcastle on February 19, 2015

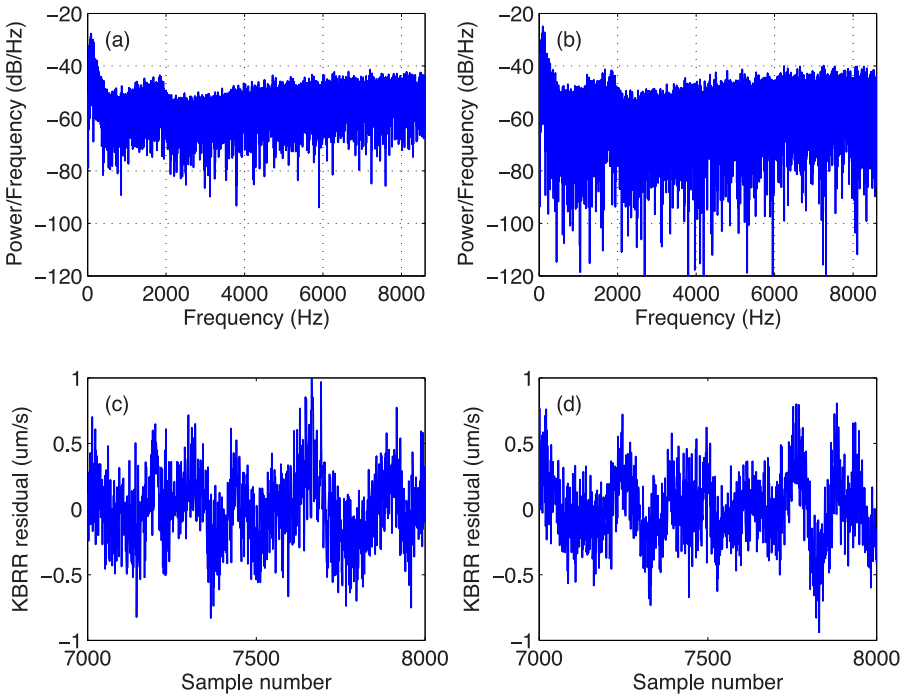

Figure 9. Periodogram of the original KBRR residual time-series (a); periodogram created from a FFT of the phase-shifted reconstructed KBRR time-series (b); sample of the original KBRR residual time-series (c); sample of the phase-shifted reconstructed KBRR residual time-series (d).

In mitigation we preserved the characterization of the error signatures but redistributed the signatures geographically by applying a fast Fourier transform (FFT) to the residual time-series. Modified KBRR residuals for each 24 hr were calculated by reconstructing the FFT through keeping the same amplitude of spectral frequency but assigning a random phase. Fig. 9 shows the original and modified FFT and KBRR residuals. Fig. 9(a) shows the original periodogram, while Fig. 9(b) shows the modified spectrum used to generate the required KBRR residuals. Fig. 9(c) shows a sample of the original KBRR residuals, while Fig. 9(d) shows the modified KBRR residuals. The original and modified KBRR residuals have similar range and noise characteristics. Fig. 9(a) shows features that are replicated in Fig. 9(b). The low frequencies (i.e. long spatial wavelengths) were investigated and characterized as flicker noise. Higher frequencies were seen to be approximately Gaussian with an increase in power between 1800 and 1900 Hz. The frequency of this signal with increased power corresponds to about twice the separation distance between the GRACE satellites. Without this artefact it would have been possible to generate the spectrum using a combination of flicker and Gaussian noise. Tests with other days and months showed that the periodogram was representative.

Tracking data, in 60 min arcs, was created with the modified KBRR residuals and the gravity field solution recovered to degree and order 60. The resulting gravity field is shown in Fig. 10 which reveals that the recovered solution is dominated by short wavelength, high degree, north–south orientated stripes; Fig. 10(b) shows the same but with 400 km Gaussian smoothing applied. The stripes are typical of those in the monthly GRACE solutions. A plot of the degree variance of the simulated stripes in Fig. 11 shows that the simulated stripes begin to dominate the signal between degree 20 and 30. Degree 30 is the degree at which regularization is normally applied to monthly solutions (Bruinsma *et al.* 2010; Save *et al.* 2012) as required to reduce the effect of noise and errors in the high degree coefficients. The power of the degree variances of the

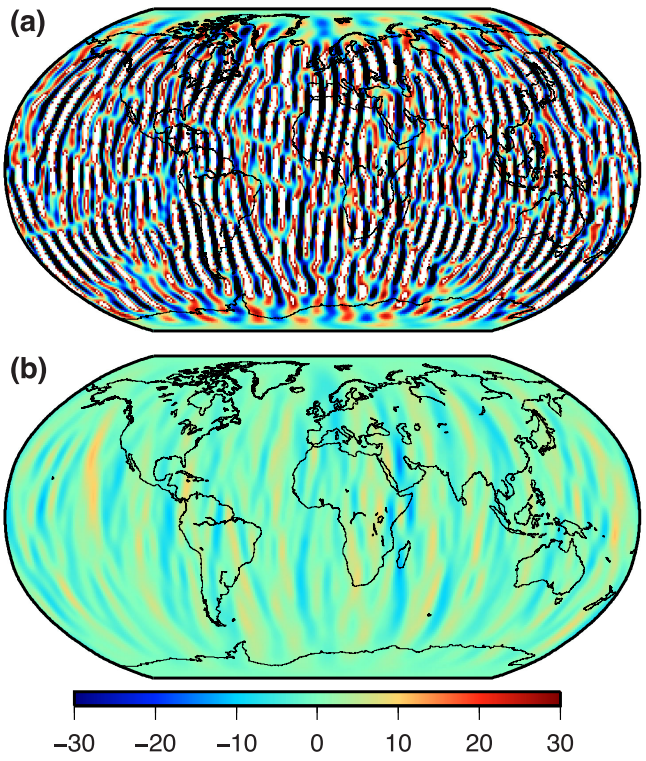

Figure 10. Simulated stripes: unsmoothed (a); with 400 km Gaussian smoothing (b). Units of cm of EWH.

simulated stripes above degree 30 was found to be comparable to those of the unsmoothed CSR solution for 2006 June. Most of the true geophysical signal is restricted to lower degrees, below degree ∼20 (Wouters & Schrama 2007) but short wavelength signals, as required for hydrological and glaciological basin-level applications,

Downloaded from http://gji.oxfordjournals.org/ at University of Newcastle on February 19, 2015

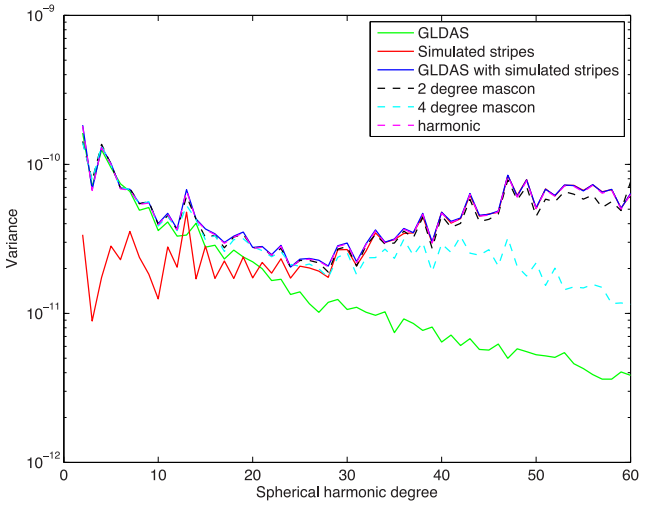

Figure 11. Degree variances of the simulated stripes, GLDAS with simulated stripes added and the unfiltered spherical harmonic and unconstrained mascon solutions. The original GLDAS model is included for comparison.

is contained in the higher degrees (Kusche 2007). This simulation thus allows us to assess the ability of the different methodologies to maintain the signal at lower degrees while reducing noise and error in the higher degrees and maximizing recovery at these shorter wavelengths.

The modified KBRR residuals were added to the original tracking data that described the GLDAS anomaly in Section 4.2. These residuals emulate the spectrum of real GRACE noise and errors with consequences that mirror the errors in actual monthly GRACE fields. The degree variances of the unconstrained solutions in Fig. 11, show that the spherical harmonic and 2° mascon solution are able to reproduce the GLDAS anomaly with simulated stripes. The global values of the 0 km (50 km) solution in Table 2 (spatial constraint mascon solutions) confirm that the simulated stripes are present in the spherical harmonic and 2° mascon solutions, with rms values of 38.1 and 35.2 cm, respectively. The 4° mascon solution is able to reproduce the degree variance of the GLDAS plus simulated stripes to degree ∼35, at which point it loses power. This loss of power, a consequence of undersampling of the signal, results in a rms of 14.7 cm in Table 2 for the 0 km solution. Again, the distance for the spherical harmonic coefficients refers to the Gaussian smoothing radius, while for the mascon solutions the distance is D of eq. (9). As previous, the distances are not directly comparable.

Regardless of the strategy used to recover the simulated field, some form of post-processing is required to reduce the effects of noise and errors in the solution. Increasing the Gaussian smoothing distance for the spherical harmonic solution reduces the rms towards the original GLDAS anomaly, with 400 km Gaussian smoothing producing the lowest rms to the GLDAS anomaly (Table 2). The global rms still reduces for 500 km Gaussian smoothing due to smoothing over the oceans, but by 500 km the land signal is over smoothed. Applying a lower smoothing radius allows the simulated stripes to dominate the solution, while a larger smoothing radius reduces the amplitude of geophysical signals and removes short wavelength information. For both the 4° and 2° mascon solutions, increasing the correlation distance D in the constraint matrix reduces the rms until ∼700 km. Over all solutions in Table 2 the 2° mascon solution provides the closest match to the GLDAS anomaly when

Table 2. Rms (cm of EWH) of the differences between the calculated gravity field solutions and input GLDAS anomalies in the presence of simulated stripes. Rms values are provided over land (globally). The distance refers to the Gaussian smoothing radius (spherical harmonic solution) or the correlation distance (mascon solutions). Mascon solution constrained using spatial (columns 3 and 4) or basin constraints (columns 5 and 6).

Distance (km)	Rms difference to GLDAS anomaly (cm EWH)				
		Spatial constraint		Basin constraint applied	
	SH coefficients	4° mascon	2° mascon	4° mascon	2° mascon
0	38.1 (37.1)	14.9 (14.7)	36.4 (35.2)	–	–
50	37.1 (35.9)	14.9 (14.7)	31.4 (30.2)	14.9 (14.7)	31.8 (30.4)
100	31.4 (30.3)	14.1 (13.6)	18.2 (17.3)	14.2 (13.7)	19.3 (17.7)
150	24.3 (23.1)	12.2 (11.1)	13.1 (11.9)	12.6 (11.2)	14.1 (12.3)
200	17.7 (16.4)	10.9 (9.2)	11.1 (9.5)	11.3 (9.3)	11.8 (9.7)
250	13.2 (11.4)	10.1 (8.0)	10.1 (8.1)	10.5 (8.1)	10.7 (8.3)
300	10.9 (8.4)	9.6 (7.3)	9.5 (7.2)	9.9 (7.4)	10.0 (7.4)
350	10.1 (6.9)	9.3 (6.7)	9.1 (6.7)	9.6 (6.8)	9.5 (6.8)
400	10.0 (6.4)	9.1 (6.4)	8.9 (6.3)	9.3 (6.4)	9.2 (6.4)
450	10.1 (6.2)	8.9 (6.1)	8.8 (6.0)	9.2 (6.2)	9.0 (6.1)
500	10.3 (6.2)	8.9 (5.9)	8.7 (5.8)	9.0 (5.9)	8.9 (5.9)
550	10.5 (6.3)	8.8 (5.8)	8.6 (5.6)	8.9 (5.8)	8.8 (5.7)
600	10.7 (6.3)	8.8 (5.7)	8.6 (5.5)	8.9 (5.6)	8.8 (5.5)
650	10.9 (6.4)	8.8 (5.6)	8.6 (5.4)	8.8 (5.5)	8.7 (5.4)
700	11.1 (6.5)	8.8 (5.5)	8.6 (5.4)	8.8 (5.5)	8.7 (5.4)
750	11.3 (6.5)	8.8 (5.5)	8.7 (5.3)	8.8 (5.4)	8.7 (5.3)
800	11.5 (6.6)	8.8 (5.4)	8.7 (5.3)	8.8 (5.3)	8.7 (5.3)
850	11.6 (6.7)	8.8 (5.4)	8.7 (5.3)	8.8 (5.3)	8.7 (5.2)
900	11.8 (6.7)	8.9 (5.4)	8.7 (5.2)	8.8 (5.3)	8.7 (5.2)
950	11.9 (6.8)	8.9 (5.4)	8.8 (5.2)	8.8 (5.3)	8.7 (5.2)
1000	12.0 (6.9)	8.9 (5.3)	8.8 (5.2)	8.8 (5.2)	8.7 (5.2)
1050	12.1 (6.9)	8.9 (5.3)	8.8 (5.2)	8.8 (5.2)	8.7 (5.1)
1100	12.2 (7.0)	9.0 (5.3)	8.9 (5.2)	8.8 (5.2)	8.8 (5.1)

Downloaded from http://gji.oxfordjournals.org/ at University of Newcastle on February 19, 2015

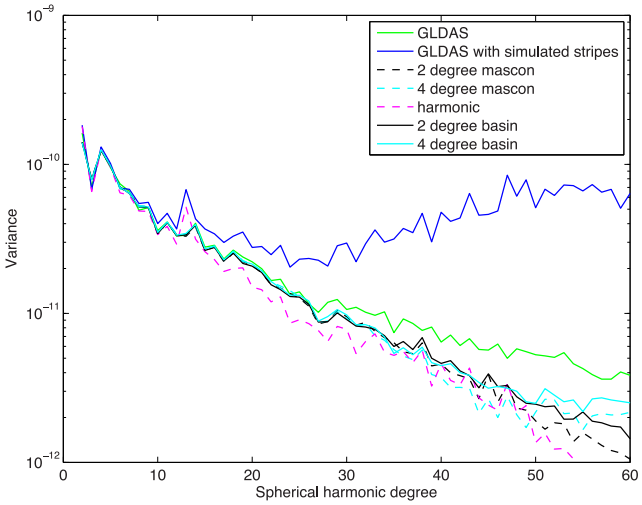

Figure 12. The degree variances of GLDAS (with and without simulated stripes) and the spherical harmonic and mascon solutions. 2° and 4° mascon are the constrained mascon solutions without the basin constraints applied while 2° and 4° basin are the constrained mascon solutions with basin constraints applied. The spherical harmonic solution has 400 km Gaussian smoothing applied; the mascon solutions are constrained using a correlation distance of 700 km in the constraint matrix (without basin constraints) and 900 km (with basin constraint).

a correlation distance of ∼650 km is used in the constraint matrix. For the 4° mascon solution we investigated the effect on the weight matrix V of varying the value of S in the eq. (9). The weight matrix V is dependent on S and D. Using $S = 0.001$, the lowest rms (8.8 cm EWH) was achieved using $D = 700$ km. When $S = 0.01$ (0.0001) were used rms values of 9.8 (10.3) were obtained. For $S = 0.01$ the lowest rms was 8.8 cm when $D = 250$ km, while for $S = 0.0001$ an rms of 9.0 cm was obtained when $D = 1500$ km. We therefore concluded, within the scope of this limited testing, that $S = 0.001$ to be the optimal scale factor for the simulations and will use this is all further processing.

Fig. 12 shows the degree variances of the spherical harmonic solution with 400 km Gaussian smoothing. It is not possible to directly relate the Gaussian smoothing distance to the mascon correlation distance so we show the mascon solutions for $D = 700$ km. This value was chosen as a comparison of the degree variances of the solutions given in Table 2 revealed it removes a comparable amount of noise to the spherical harmonic solution at the higher degrees. It also gives one of the lowest rms values to the GLDAS anomaly. Fig. 12 reveals that all solutions have removed a similar amount of noise and error above degree 30, and contain less power at these degrees compared to the GLDAS signal. The mascon solutions more closely resemble the power of the GLDAS signal between ∼degree 15 and 30 than the spherical harmonic solution. The reduced power of the spherical harmonic signal between ∼degree 15 and 30 could be partly related to the degree dependency of the Gaussian filter which Han *et al.* (2005) suggested could suppress information over this range. The mascon solution has therefore been able to recover more of the original signal at degrees ∼15–30 while removing a comparable amount of noise and error at higher degrees.

4.6 Basin constraints

Mascon solutions with spatial constraints are able to remove more noise and error and retain more signal than spherical harmonics solutions with Gaussian smoothing. However, thus far we have not exploited the full advantage of the mascon processing strategy; namely that the constraint matrix in eq. (5) can be adapted to constrain mascons that share geophysical similarities as in Luthcke *et al.* (2006b). Thus, in addition to separating mascons into either land or ocean, we now also separate the major hydrological drainage basins defined by the total runoff integrating pathways (TRIP) data set (Oki & Sud 1998). Major Greenland and Antarctic drainage basins are adopted according to Zwally *et al.* (2012). The result is a constraint matrix where constraints are imposed between all land mascons within the same (hydrological or glaciological) drainage basin, with mascons in different basins uncorrelated. Not all land mascons are within a major hydrological or glaciological basin. Land mascons that are not classified as belonging to a basin were assumed to be correlated, but in most instances d_{IJ} of eq. (8) or (9) reduces the correlation to ∼0. All ocean mascons are correlated as previous.

Table 2 (Basin constraint mascon solutions) summarizes the rms of the differences to the GLDAS plus simulated stripes. For both mascon solutions the use of a basin constraint, while offering a similar or small improvement in the rms over land, offers an improvement in global rms values over the solutions without basin constraints. An increase in the correlation distance (800–900 km) is required to obtain these improvements due to the reduced number of constraints based on mascons pairs that share geophysical similarities. The improved global rms is due to reduction of the simulated stripes over the ocean. As ocean mascons are constrained together, the increased correlation distance allows the effect of the simulated stripes to be further mitigated. The improvement is evident in the degree variances of the mascon solutions (basin) plotted in Fig. 12. Comparing mascon solutions with and without basin constraints, the power of the resulting mascon solutions from degrees 30 to 60 more closely matches the input signal when the basin constraint is applied. The constraints have successfully reduced the noise at these degrees while reducing loss of actual signal. Retention of short wavelength signal is of fundamental importance for improving basin-scale hydrological and glaciological recovery and for estimating basin-level mass flux.

The final recovered GLDAS anomalies are shown in Fig. 13 for the spherical harmonic solution with 400 km Gaussian smoothing together with the 2° mascon solution using a 800 km correlation distance and basin constraints. The input GLDAS anomaly is provided for reference. Comparing Figs 13(c) to (a) validates the 2° mascon solution. The mascon methodology offers a clear improvement in the recovery of TVG and suppression of simulated stripes compared with a spherical harmonic solution with Gaussian smoothing. The reduction of the simulated stripes over the ocean is particularly evident. Unlike spherical harmonics, mascons allow constraints within areas that share real world geophysical properties. Any number of constraints can be applied with the aim of improving the overall recovery of the TVG field.

4.7 Simulated recovery of Antarctic mass change signal

One of the scientific advances provided by the GRACE mission is recovery of continent-wide ice sheet mass change estimates, such as over Antarctica, with temporal resolutions of 30 days or less. So far our simulations have focused on recovery of a GLDAS hydrological anomaly. Given the scientific interest in contribution of ice sheets to sea-level change and the convergence of orbital tracks at the pole we now simulate recovery of a realistic Antarctica mass signal along with the GLDAS anomaly and error/noise product

Downloaded from http://gji.oxfordjournals.org/ at University of Newcastle on February 19, 2015

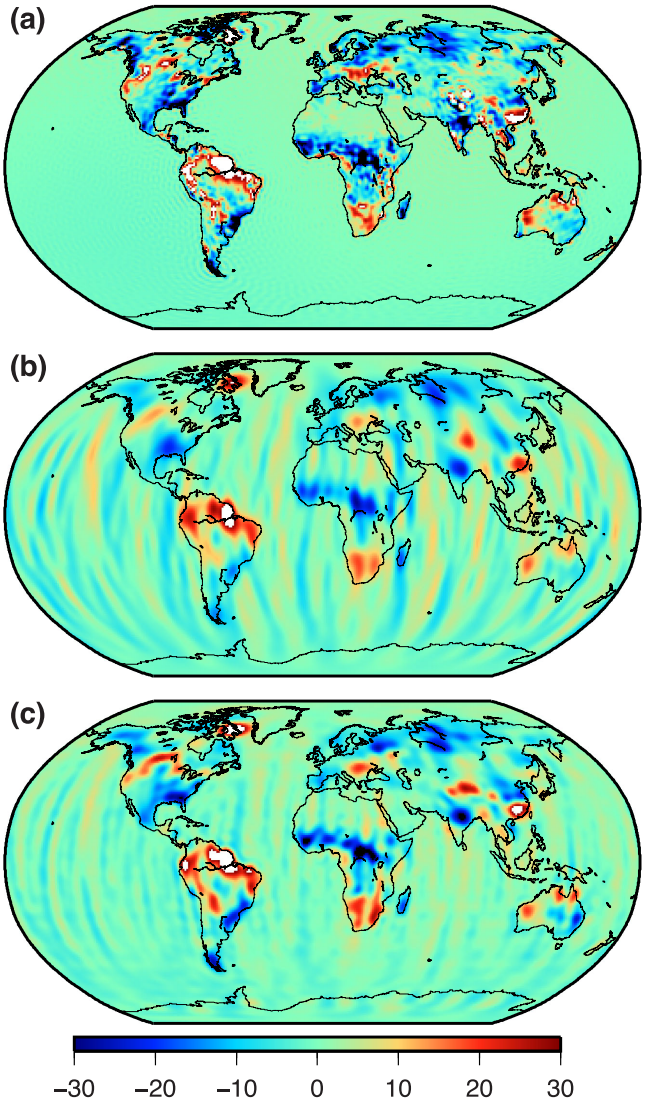

Figure 13. GLDAS anomaly for 2006 June to degree and order 120 (a); Recovered GLDAS anomalies for the spherical harmonic solution with 400 km Gaussian smoothing to degree and order 60 (b); and 2° mascon solution with a basin constraint applied, with 800 km correlation distance (c). Units of cm EWH.

described in Section 4.5. The simulated Antarctica mass signal was derived from the basin mass change rates provided in Table S1 of the supplementary material of King *et al.* (2012). While King *et al.* (2012) calculated GRACE solutions to degree and order 60, forward modelling across defined basins resulted in a higher effective resolution. The mass change rates used have been corrected for leakage but still contain the GIA signal that is observable from GRACE. Using the same drainage basins adopted by King *et al.* (2012), as defined using ICESat data (Zwally *et al.* 2012), the mass change rates for each basin were converted to a total mass change in cm of EWH using the density of water and the area of each drainage basin. As in King *et al.* (2012) basins 25 and 26, which cover the northern tip of the Antarctica Peninsula, were merged into a single basin. The resulting mass changes for each basin were then expanded into spherical harmonics to degree and order 60 and added to the mean background field to create the KBRR tracking data. Simulated stripes are included as previous. The simulated Antarctic mass change signal can be seen in Fig. 14. Plotting the unfiltered

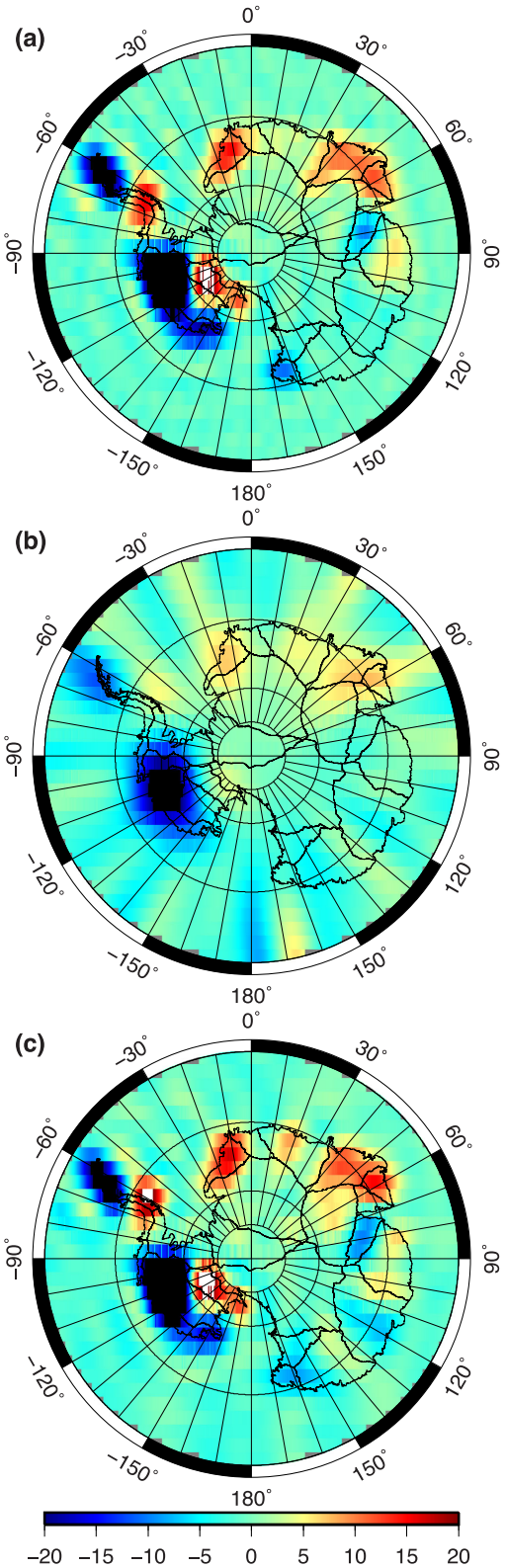

Figure 14. Simulated Antarctic mass change signal (a); spherical harmonic solution filtered with a 350 km Gaussian smoother (b); and 2° mascon solution with basin constraint with correlation distance $D = 800$ km (c). Units of cm of EWH.

Downloaded from http://gji.oxfordjournals.org/ at University of Newcastle on February 19, 2015

Table 3. Rms (cm of EWH) of the differences between the calculated gravity field solutions and the input GLDAS anomaly with Antarctic mass change signal in the presence of different simulated noise products. Rms values are provided over land (and globally). The distance refers to the Gaussian smoothing radius (spherical harmonic coefficient solutions) or the correlation distance (mascon solutions). All mascon solutions utilize basin constraints described in Section 4.6. For the thermal mascon solutions the value S in eq. (9) was increased from 0.001 to 0.01.

Distance (km)	Rms difference to GLDAS anomaly and Antarctic mass change (cm EWH)					
	Main period		Resonance period		Reduced thermal control	
	SH	2° mascon	SH	2° mascon	SH	2° mascon
200	17.7 (16.4)	11.8 (9.8)	20.3 (19.8)	8.1 (5.3)	45.2 (45.5)	13.9 (11.0)
250	13.2 (11.4)	10.7 (8.3)	14.8 (13.8)	8.0 (5.0)	29.9 (29.7)	12.4 (9.3)
300	10.9 (8.4)	10.0 (7.4)	11.6 (9.8)	8.0 (4.9)	20.6 (19.5)	11.7 (8.2)
350	10.1 (7.0)	9.5 (6.8)	10.3 (7.6)	8.0 (4.9)	15.6 (13.7)	11.3 (7.6)
400	10.0 (6.4)	9.2 (6.4)	10.0 (6.6)	8.1 (4.9)	13.2 (10.6)	11.0 (7.2)
450	10.2 (6.3)	9.0 (6.1)	10.1 (6.2)	8.2 (4.9)	12.2 (9.0)	10.9 (7.0)
500	10.4 (6.3)	8.9 (5.9)	10.3 (6.2)	8.3 (4.9)	11.7 (8.1)	10.8 (6.8)
550	10.6 (6.3)	8.8 (5.7)	10.6 (6.2)	8.3 (4.9)	11.6 (7.6)	10.8 (6.6)
600	10.8 (6.4)	8.8 (5.5)	10.8 (6.3)	8.4 (4.9)	11.6 (7.4)	10.8 (6.6)
650	11.0 (6.4)	8.7 (5.4)	11.1 (6.4)	8.5 (5.0)	11.6 (7.2)	10.8 (6.5)
700	11.2 (6.5)	8.7 (5.4)	11.3 (6.5)	8.6 (5.0)	11.7 (7.2)	10.8 (6.5)
750	11.4 (6.6)	8.7 (5.3)	11.5 (6.6)	8.6 (5.0)	11.8 (7.1)	10.9 (6.4)
800	11.6 (6.7)	8.7 (5.3)	11.7 (6.7)	8.7(5.0)	11.9 (7.1)	10.9 (6.4)
850	11.7 (6.7)	8.7 (5.2)	11.8 (6.8)	8.8 (5.1)	12.0 (7.1)	11.0 (6.4)
900	11.9 (6.8)	8.7 (5.2)	12.0 (6.9)	8.8 (5.1)	12.1 (7.1)	11.0 (6.4)
950	12.0 (6.9)	8.7 (5.2)	12.1 (6.9)	8.9 (5.1)	12.2 (7.1)	11.1 (6.4)
1000	12.1 (6.9)	8.7 (5.2)	12.2 (7.0)	9.0 (5.2)	12.3 (7.2)	11.1 (6.4)
1050	12.2 (7.0)	8.7 (5.1)	12.3 (7.0)	9.0 (5.2)	12.3 (7.2)	11.2 (6.5)
1100	12.3 (7.0)	8.8 (5.1)	12.4 (7.1)	9.1 (5.2)	12.4 (7.2)	11.2 (6.5)

degree variances (not shown) reveals that the spherical harmonic and 2° mascon solution were able to reproduce the Antarctica mass signal added to the GLDAS anomaly and simulated stripes. Application of a single value of mass change per basin is a simplification on the real spatial pattern of change, but this assumption is sufficient for our purposes here.

Solutions were estimated for the spherical harmonics and 2° mascon methodologies with the rms values shown in Table 3 (main period). The drainage basins used in the mascon solution in Section 4.6 result in mascons within the same Antarctic drainage basin being constrained together, but with mascons in different Antarctic basins uncorrelated. The mascon results are shown in Fig. 14(c) revealing this solution has been able to recover most of the input signal (Fig. 14a) while the spherical harmonic solution filtered with 400 km Gaussian smoothing (Fig. 14b) has recovered the spatial extent of the signal but with reduced amplitudes. This is important to consider within future GRACE studies of Antarctic ice mass change. The lowest rms of the differences to the input signal (in EWH) over Antarctica is 8.7 cm for the mascon solution (800 km correlation distance) and 10.4 cm with spherical harmonics (400 km Gaussian smoothing). As with the global hydrological simulations, we are able to recover more of the signal using the mascon methodology.

As a final comparison we computed the mascon solution with only land/ocean constraints as applied in Section 4.5. The rms of the difference to the input Antarctica signal was 8.8 cm. This highlights the advantage offered by the mascon methodology when real-world geophysical properties are used to define the constraints between the mascons. We note, however, that a simple basin-wide constraint may not be an accurate reflection of changes within a basin and more sophisticated treatment, such as increasing the numbers of basins (e.g. Luthcke *et al.* 2013) based on ice dynamic considerations, may further improve analysis of real GRACE data.

4.8 GRACE resonance and thermal control issues

Periods where the GRACE satellites are in 3, 4 and 7 day repeat orbits modify the noise characteristics of the GRACE solutions (Save *et al.* 2012), while recent GRACE solutions are affected by poor satellite thermal control. For replicating the GRACE errors and studying the correlations between the spherical harmonic coefficients in CSR RL05 solutions, covariance matrices are provided by CSR for the three characteristic periods in the GRACE mission: early mission (2002 February–2005 May), main part of the mission (2007 July–2010 December) and recent months (2011 February–) which are affected by poor thermal control. Only three covariance matrices are required as the monthly variations within these periods are minor as to be unimportant (John C Ries, personal communication, 2014). An additional covariance matrix is available for months where the satellite is in a repeat orbit (resonance). The effect these different periods have on the noise and errors is investigated through recovery of the GLDAS anomaly and Antarctica mass change signal for two additional sets of simulated noise. The GLDAS anomaly and Antarctica mass change signal are the same as in previous simulations. The first set of simulated noise relates to September 2004, when the GRACE satellites were in 61:4 resonance (Klokočník *et al.* 2013). The second set relates to 2011 March, which corresponds to a period when the GRACE satellites are affected by poor thermal control. KBRR residuals for 2004 September and 2011 March with simulated noise were derived using the method of Section 4.5. We computed the modified FFT and KBRR residuals for 2004 September and 2011 March (as in Fig. 9). For 2004 September (not shown) these revealed that the noise and errors in GRACE during resonance are indistinguishable from that of the main part of the mission. The 2011 March residuals are shown in Fig. 15, revealing an increase in the amplitude of the KBRR residuals; compare Figs 15(c) and (d) with Figs 9(c) and (d). This increase in amplitude is the result of

Downloaded from http://gji.oxfordjournals.org/ at University of Newcastle on February 19, 2015

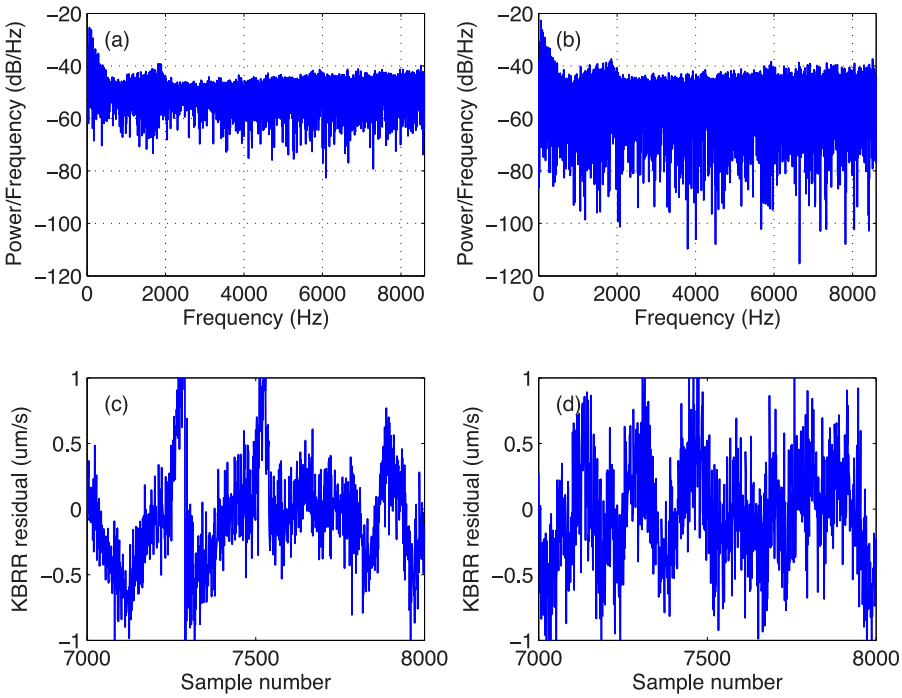

Figure 15. Periodogram of the poor thermal control KBRR residual time-series (a) and FFT phase shifted reconstructed KBRR time-series (b); sample of the poor thermal control KBRR residual time-series (c); sample of the reconstructed KBRR residual time-series (d).

the poor thermal control, which we would expect to increase from 2011 onwards.

Table 3 summarizes the rms of the difference to the GLDAS and Antarctica mass loss signal in the presence of simulated stripes from three periods (main, resonance and thermal control). The simulated stripes for the main period are described in Section 4.5. The rms values are provided for the spherical harmonic and 2° mascon solutions. In the resonance period, increasing the Gaussian smoothing until 400 km reduces the rms at which point the signal recovered is comparable to the main period; the larger global rms suggests more of the stripes remain over the oceans. For the mascon solution the lowest rms obtained is obtained when a correlation distance of 250 km is used, which is a much lower than the distance required for the 2006 June simulation of the main period. The rms is also much lower, suggesting the mascon methodology is able to deal well with periods of resonance. In 61:4 resonance the satellite ground-track repeats every 61 orbital revolutions in the time the Earth revolves 4 times relative to the ascending node. This gives 122 repeating ascending and descending passes every 4 days spaced on average every 3° in longitude. This spatial resolution is adequate for a spherical harmonic field to degree and order 60. Similarly, a mascon correlation distance of 250 km, equivalent to the distance between centres of 2° equatorial mascons, provides the ties between neighbouring mascons. It would appear that the resonance facilitates separation of spatial and temporal errors in our simulation leading to more accurate surface mass recovery than in non-resonant periods.

In the period of reduced thermal control both the spherical harmonic and mascon solutions are degraded. The lowest rms (11.6 cm EWH) for the spherical harmonic solution is obtained with 600 km Gaussian smoothing. Even with this smoothing radius, the rms obtained is larger than for the main and resonance periods. For the mascon solution, the lowest rms (10.8) is obtained with a correlation distance $D = 600$ km, compared to 8.7 (8.0) for the solutions with the original (resonance) noise. To achieve this rms the value S in eq. (9) was increased from 0.001 to 0.01 which increases the effect the constraint matrix has on the solution. For both the mascon and spherical harmonic solutions a larger constraint matrix is required to deal with the noise and errors resulting from the poor thermal control. While the recovery in the presence of the thermal stripes is not as favourable for both methodologies, when compared to the original or resonance periods, the mascon methodology is still able to recover more of the input signal than the spherical harmonic methodology while also reducing the noise over the ocean.

5 CONCLUSION

Through the use of simulations we have demonstrated the sensitivity of GRACE to mass over a large area, with the effect on the KBRR residuals depending on the amplitude of the signal. Building on this we showed that recovery of global mass distributions require contributions to the satellite accelerations of all mascons within approximately 6000 km of the nadir mascon. This has implications when estimating a non-global mascon solution, and is useful in reducing computational effort for high resolution global mascon solutions. We found that the use of iterations cannot compensate for an insufficient distribution of mascons.

Simulated recovery of a noise and error free GLDAS mass anomaly showed that there is no quantifiable difference between a mass anomaly solution recovered from KBRR data using spherical harmonics and a 2° equal area mascon solution; both recovered the input GLDAS anomaly. A 4° mascon solution does not have the required resolution to recover the gravity field solution to degree and order 60 due to the number of mascon parameters estimated being less than the gravity field parameters required; this causes a loss of higher degree information in the gravity field. Recovery of the GLDAS mass anomaly described to degree and order 120 revealed that all methodologies are affected by omission errors, with

Downloaded from http://gji.oxfordjournals.org/ at University of Newcastle on February 19, 2015

the additional short wavelength (high degree) information not being captured.

The recovery of the GLDAS anomaly with simulated stripes reveals the advantage of the mascon solution over a spherical harmonic solution smoothed with a Gaussian filter when attempting to reduce high degree and order noise. The use of the mascon spatial constraint matrix allowed more signal to be preserved up to degree ∼35, while the addition of constraints between mascon parameters that share geophysical similarities resulted in a further reduction of the lost signal at all degrees. This improvement is further evident in the simulated recovery of the Antarctic mass signal which also confirms the advantage of the mascon solution over the spherical harmonic recovery validating the use of this methodology in polar regions. Inclusion of temporal constraints could result in further improvements, but a level of assumption would be required on plausible variations of mass over time.

The recovery of the GLDAS anomaly and Antarctica mass change signal with simulated stripes, created during periods when GRACE was in resonance and suffering from poor thermal control, revealed that in both cases the mascon methodology was able to recover more of the input signal than using spherical harmonic methodology. This advantage was especially evident during periods of resonance. The use of the mascon methodology also reduced the effect of stripes over the ocean. However, both the spherical harmonic and mascon solutions were degraded during periods of reduced thermal control. In particular, the reduced thermal control necessitated tighter constraints between the various mascons than during the main part of the mission.

Finally, while the values used for S and D were found to be optimal in this paper, they may differ for users depending on parametrization, and are therefore provided as a guide. Furthermore, adaptations to the S and D values appear to be necessary as the GRACE mission ages.

ACKNOWLEDGEMENTS

This work was funded by a National Centre for Earth Observation (NCEO) award in gravimetric geodesy and partially supported by COST Action ES0701 'Improved constraints on models of Glacial Isostatic Adjustment'. We are gratefully for the GRACE Level-1B products produced by the Jet Propulsion Laboratory. MAK is a recipient of an Australian Research Council Future Fellowship (project number FT110100207). The authors would like to thank three anonymous reviewers for comments which helped improve this manuscript.

REFERENCES

Awange, J.L., Fleming, K.M., Kuhn, M., Featherstone, W.E., Heck, B. & Anjasmara, I., 2011. On the suitability of the 4 degree x 4 degree GRACE mascon solutions for remote sensing Australian hydrology, *Rem. Sens. Environ.,* **115,** 864–875.

Bettadpur, S., 2012. *UTCSR Level-2 Processing Standards Document for Level-2 Product Release 0005,* pp. 16, GRACE 327–742. University of Texas at Austin, CSR Publ: GR-12-xx, Rev. 4.0.

Bruinsma, S., Lemoine, J.-M., Biancale, R. & Valès, N., 2010. CNES/GRGS 10-day gravity field models (release 2) and their evaluation, *Adv. Space Res.,* **45,** 587–601.

Chambers, D.P. & Bonin, J.A., 2012. Evaluation of release-05 GRACE time-variable gravity coefficients over the ocean, *Ocean Sci.,* **8,** 859–868.

Chambers, D.P., Wahr, J., Tamisiea, M.E. & Nerem, R.S., 2010. Ocean mass from GRACE and glacial isostatic adjustment, *J. geophys. Res.,* **115,** B11415, doi:10.1029/2010JB007530.

Chen, J.L., Wilson, C.R., Tapley, B.D., Blankenship, D. & Young, D., 2008. Antarctic regional ice loss rates from GRACE, *Earth planet. Sci. Lett.,* **266,** 140–148.

Dunn, C. *et al.*, 2003. Instrument of GRACE: GPS augments gravity measurements, *GPS World,* **14,** 16–28.

Farrell, W.E., 1972. Deformation of earth by surface loads, *Rev. Geophys. Space Phys.,* **10,** 761–797.

Han, S.-C., Shum, C.K., Jekeli, C., Kuo, C.-Y., Wilson, C. & Seo, K.-W., 2005. Non-isotropic filtering of GRACE temporal gravity for geophysical signal enhancement, *Geophys. J. Int.,* **163**(1), 18–25.

Han, S.-C., Sauber, J., Luthcke, S.B., Ji, C. & Pollitz, F.F., 2008. Implications of postseismic gravity change following the great 2004 Sumatra-Andaman earthquake from the regional harmonic analysis of GRACE intersatellite tracking data, *J. geophys. Res.: Solid Earth,* **113,** B11413, doi:10.1029/2008JB005705.

Han, S.-C., Kim, H., Yeo, I.-Y., Yeh, P., Oki, T., Seo, K.-W., Alsdorf, D. & Luthcke, S.B., 2009. Dynamics of surface water storage in the Amazon inferred from measurements of inter-satellite distance change, *Geophys. Res. Lett.,* **36,** L09403, doi:10.1029/2009GL037910.

Jacob, T., Wahr, J., Pfeffer, W.T. & Swenson, S., 2012. Recent contributions of glaciers and ice caps to sea level rise, *Nature,* **482,** 514–518.

King, M.A., Bingham, R.J., Moore, P., Whitehouse, P.L., Bentley, M.J. & Milne, G.A., 2012. Lower satellite-gravimetry estimates of Antarctic sea-level contribution, *Nature,* **491,** 586–589.

Klees, R., Revtova, E.A., Gunter, B.C., Ditmar, P., Oudman, E., Winsemius, H.C. & Savenije, H.H.G., 2008. The design of an optimal filter for monthly GRACE gravity models, *Geophys. J. Int.,* **175,** 417–432.

Klokočník, J., Gooding, R.H., Wagner, C.A., Kostelecký, J. & Bezděk, A., 2013. The use of resonant orbits in satellite geodesy: a review, *Surv. Geophys.,* **34,** 43–72.

Klosko, S., Rowlands, D., Luthcke, S., Lemoine, F., Chinn, D. & Rodell, M., 2009. Evaluation and validation of mascon recovery using GRACE KBRR data with independent mass flux estimates in the Mississippi Basin, *J. Geod.,* **83,** 817–827.

Kusche, J., 2007. Approximate decorrelation and non-isotropic smoothing of time-variable GRACE-type gravity field models, *J. Geod.,* **81,** 733–749.

Lemoine, F.G., Luthcke, S.B., Rowlands, D.D., Chinn, D.S., Klosko, S.M. & Cox, C.M., 2007. The use of mascons to resolve time-variable gravity from GRACE, in *Dynamic Planet,* pp. 231–236, eds Tregoning, P. & Rizos, C., Springer.

Luthcke, S.B., Rowlands, D.D., Lemoine, F.G., Klosko, S.M., Chinn, D. & McCarthy, J.J., 2006a. Monthly spherical harmonic gravity field solutions determined from GRACE inter-satellite range-rate data alone, *Geophys. Res. Lett.,* **33,** L02402, doi:10.1029/2005GL024846.

Luthcke, S.B. *et al.*, 2006b. Recent Greenland ice mass loss by drainage system from satellite gravity observations, *Science,* **314,** 1286–1289.

Luthcke, S.B., Arendt, A.A., Rowlands, D.D., McCarthy, J.J. & Larsen, C.F., 2008. Recent glacier mass changes in the Gulf of Alaska region from GRACE mascon solutions, *J. Glaciol.,* **54,** 767–777.

Luthcke, S.B., Sabaka, T.J., Loomis, B.D., Arendt, A.A., McCarthy, J.J. & Camp, J., 2013. Antarctica, Greenland and Gulf of Alaska land-ice evolution from an iterated GRACE global mascon solution, *J. Glaciol.,* **59,** 613–631.

Moore, P., Boomkamp, H.J., Carnochan, S. & Walmsley, R.J., 1999. FAUST: multi-satellite orbital dynamics software, *Adv. Space Res.,* **23,** 785–795.

Muller, P.M. & Sjogren, W.L., 1968. Mascons: lunar mass concentrations, *Science,* **161,** 680–684.

Oki, T. & Sud, Y.C., 1998. Design of total runoff integrating pathways (TRIP)—a global river channel network, *Earth Interact.,* **2,** 1–37.

Pritchard, H.D., Luthcke, S.B. & Fleming, A.H., 2011. Understanding ice-sheet mass balance: progress in satellite altimetry and gravimetry, *J. Glaciol.,* **56,** 1151–1161.

Ramillien, G., Biancale, R., Gratton, S., Vasseur, X. & Bourgogne, S., 2011. GRACE-derived surface water mass anomalies by energy integral approach: application to continental hydrology, *J. Geod.,* **85,** 313–328.

Downloaded from http://gji.oxfordjournals.org/ at University of Newcastle on February 19, 2015

Ries, J.C., Bettadpur, S., Poole, S. & Richter, T., 2011. Mean background gravity fields for GRACE processing, in *Proceedings of the GRACE Science Team Meeting,* Austin, TX.

Riva, R.E.M. *et al.*, 2009. Glacial isostatic adjustment over Antarctica from combined ICESat and GRACE satellite data, *Earth planet. Sci. Lett.,* **288,** 516–523.

Rodell, M. *et al.*, 2004. The global land data assimilation system, *Bull. Am. Meteor. Soc.,* **85**(3), 381–394.

Rowlands, D.D., Ray, R.D., Chinn, D.S. & Lemoine, F.G., 2002. Short-arc analysis of intersatellite tracking data in a gravity mapping mission, *J. Geod.,* **76,** 307–316.

Rowlands, D.D., Luthcke, S.B., Klosko, S.M., Lemoine, F.G.R., Chinn, D.S., McCarthy, J.J., Cox, C.M. & Anderson, O.B., 2005. Resolving mass flux at high spatial and temporal resolution using GRACE intersatellite measurements, *Geophys. Res. Lett.,* **32,** L04310, doi:10.1029/2004GL021908.

Rowlands, D.D., Luthcke, S.B., McCarthy, J.J., Klosko, S.M., Chinn, D.S., Lemoine, F.G., Boy, J.P. & Sabaka, T.J., 2010. Global mass flux solutions from GRACE: a comparison of parameter estimation strategies—mass concentrations versus Stokes coefficients, *J. geophys. Res.,* **115,** B01403, doi:10.1029/2009JB006546.

Sabaka, T.J., Rowlands, D.D., Luthcke, S.B. & Boy, J.P., 2010. Improving global mass flux solutions from Gravity Recovery and Climate Experiment (GRACE) through forward modeling and continuous time correlation, *J. geophys. Res.,* **115,** B11403, doi:10.1029/2010JB007533.

Save, H., Bettadpur, S. & Tapley, B., 2012. Reducing errors in the GRACE gravity solutions using regularization, *J. Geod.,* **86,** 695–711.

Schrama, E.J.O. & Wouters, B., 2011. Revisiting Greenland ice sheet mass loss observed by GRACE, *J. geophys. Res.,* **116,** B02407, doi:10.1029/2009JB006847.

Schrama, E.J.O., Wouters, B. & Rietbroek, R., 2014. A mascon approach to assess ice sheet and glacier mass balances and their uncertainties from GRACE data, *J. geophys. Res.: Solid Earth,* **119,** 6048–6066.

Seo, K.W., Wilson, C.R., Famiglietti, J.S., Chen, J.L. & Rodell, M., 2006. Terrestrial water mass load changes from Gravity Recovery and Climate Experiment (GRACE), *Water Resour. Res.,* **42,** W05417, doi:10.1029/2005WR004255.

Seo, K.-W., Wilson, C.R., Chen, J. & Waliser, D.E., 2008. GRACE's spatial aliasing error, *Geophys. J. Int.,* **172,** 41–48.

Shepherd, A. *et al.*, 2012. A reconciled estimate of ice-sheet mass balance, *Science,* **338,** 1183–1189.

Swenson, S. & Wahr, J., 2002. Methods for inferring regional surface-mass anomalies from Gravity Recovery and Climate Experiment (GRACE) measurements of time-variable gravity, *J. geophys. Res.,* **107,** 2193, doi:10.1029/2001JB000576.

Swenson, S. & Wahr, J., 2006. Post-processing removal of correlated errors in GRACE data, *Geophys. Res. Lett.,* **33,** L08402, doi:10.1029/2005GL025285.

Tapley, B.D., Bettadpur, S., Ries, J.C., Thompson, P.F. & Watkins, M.M., 2004a. GRACE measurements of mass variability in the Earth system, *Science,* **305,** 503–505.

Tapley, B.D., Bettadpur, S., Watkins, M. & Reigber, C., 2004b. The gravity recovery and climate experiment: mission overview and early results, *Geophys. Res. Lett.,* **31,** 503–505.

Velicogna, I. & Wahr, J., 2006. Measurements of time-variable gravity show mass loss in Antarctica, *Science,* **311,** 1754–1756.

Wahr, J., Molenaar, M. & Bryan, F., 1998. Time variability of the Earth's gravity field: hydrological and oceanic effects and their possible detection using GRACE, *J. geophys. Res.,* **103,** 30 205–30 229.

Wahr, J., Swenson, S. & Velicogna, I., 2006. Accuracy of GRACE mass estimates, *Geophys. Res. Lett.,* **33,** L06401, doi:10.1029/2005GL025305.

Wahr, J., Swenson, S., Zlotnicki, V. & Velicogna, I., 2004. Time-variable gravity from GRACE: first results, *Geophys. Res. Lett.,* **31,** L11501, doi:10.1029/2004GL019779.

Wouters, B. & Schrama, E.J.O., 2007. Improved accuracy of GRACE gravity solutions through empirical orthogonal function filtering of spherical harmonics, *Geophys. Res. Lett.,* **34,** L23711, doi:10.1029/2007GL032098.

Wouters, B., Chambers, D. & Schrama, E.J.O., 2008. GRACE observes small-scale mass loss in Greenland, *Geophys. Res. Lett.,* **35,** L20501, doi:10.1029/2008GL034816.

Zwally, H.J., Giovinetto, M.B., Beckley, M.A. & Sab, J.L., 2012. Antarctic and Greenland drainage systems, GSFC Cryospheric Sciences Laboratory, Available at: http://icesat4.gsfc.nasa.gov/cryo_data/ant_grn_drainage_systems.php, last accessed 9 December 2013.

Downloaded from http://gji.oxfordjournals.org/ at University of Newcastle on February 19, 2015